Uniaxial anisotropy and low-temperature antiferromagnetism of Mn₂BO₄ single crystal

N.V. Kazak [a,*], M.S. Platunov [a], Yu.V. Knyazev [b], N.B. Ivanova [b], O.A. Bayukov [a], A.D. Vasiliev [a,b], L.N. Bezmaternykh [a], V.I. Nizhankovskii [d], S.Yu. Gavrilkin [e], K.V. Lamonova [f], S.G. Ovchinnikov [a,b,c]

[a] L.V. Kirensky Institute of Physics, SB of RAS, Academgorodok 50/38, 660036 Krasnoyarsk, Russia
[b] Siberian Federal University, 660074 Krasnoyarsk, Russia
[c] Siberian State Aerospace University, 660014 Krasnoyarsk, Russia
[d] International Laboratory of High Magnetic Fields and Low Temperatures, PL-53421 Wroclaw, Poland
[e] P.N. Lebedev Physical Institute of RAS, 119991 Moscow, Russia
[f] O.O. Galkin Donetsk Institute for Physics and Engineering, National Academy of Sciences of Ukraine, 83114 Donetsk, Ukraine

ARTICLE INFO

ABSTRACT

The Mn₂BO₄ single crystals have been grown by the flux technique. A careful study of the crystal structure and magnetic properties have been carried out. The antiferromagnetic transition at $T_N=26$ K has been traced through the *dc* magnetization and specific heat temperature dependences. Magnetic uniaxial anisotropy has been found with easy axis magnetization lying in the ab-plane. The obtained value of effective magnetic moment is assigned to the non-quenched orbital moment of Jahn–Teller Mn^{3+} ions. The discussion of magnetic properties is based on the superexchange interaction calculations.

© 2015 Elsevier B.V. All rights reserved.

1. Introduction

It is well known that low dimensionality in crystal and magnetic structure plays an important role in the physics of magnetic crystals. The experimental and theoretical investigations have revealed properties of the materials with low dimensionality to be quite different from their bulk analogs. This difference results in the rich variety of phases and phase transitions caused by high degree of degeneration and extraordinary sensitivity to external influences. From this point of view the borates of transition and rare-earth metals with quasi-low dimension crystal structure and unique magnetic and optic properties are the perspective objects for the fundamental and practical investigations. These materials form a wide class of narrow-band oxide semiconductors intensely studied recently [1–5].

The oxyborates $M^{2+}M^{3+}BO_4$ with the warwickite structure attract attention due to a large number of isomorphic substitutions. There is a large variety of natural and synthetic warwickites containing rare-earth, alkaline earth and transition metal ions

($M^{2+}=$ Mg, Co, Mn, Fe, and Ni, and $M^{3+}=$ Ti, V, Cr, Fe, Mn, In, Lu, Yb, and Tm) [6–8]. The metal ions occupy two structurally distinct octahedral sites usually labeled as 1 and 2. Four octahedra linked by sharing edges form the *row* of 2-1-1-2. The *rows* are connected by sharing edges forming quasi low-dimensional *ribbons* extending along crystalline *c*-axis. The heterometallic warwickites ($M^{2+}\neq M^{3+}$) are naturally disordered materials since each cation site may be occupied by any one of the two metals. Most heterometallic warwickites show typical spin-glass transition [6,9].

Recently, we have performed the crystal structure, magnetic and electronic studies of $Mg_{1-x}Co_xBO_4$ ($x=0.0$, 0.5, and 1.0) single crystals [10–13]. Mössbauer and magnetization studies have shown spin-glass behavior and quantum entanglement behavior $\chi(T)\infty T^{-\alpha(T)}$ above T_{SG}. The Co induced magnetocrystaline anisotropy increases the magnetic viscosity of the magnetic lattice, by freezing magnetic fluctuations below T_{SG}. On the contrary, the introduction of Cobalt does not alter transport properties radically.

Only two homometallic warwickites ($M^{2+}=M^{3+}$) are available now: Fe₂BO₄ and Mn₂BO₄ [14,15]. Both compounds display charge ordering (CO). The nature of CO in the warwickites is the subject of hot discussions. The temperature dependence of CO in Fe₂BO₄ was extensively investigated by resistivity and differential scanning

calorimetry measurements, Mössbauer spectroscopy, synchrotron x-ray scattering, transmission electron microscopy, and electronic-structure calculations [16–19]. It has been proposed that the low-temperature phase $(T_{CCO} < 280\ K)$ is a commensurately charge ordered with integer iron valence separation Fe^{2+} and Fe^{3+} alternating in the a-axis direction. The intermediate temperature range $(T_{CCO} < T < T_{CO}$, where $T_{CO} = 340\ K)$ is characterized by the onset of the temperature-dependent lattice incommensurate CO accompanied by coexisting mobile and immobile carriers. There is a valence fluctuating state (Fe^{2+}–Fe^{3+} electron hopping) in the high-temperature interval $(T > T_{CO})$ where the structural transformation from monoclinic→orthorhombic symmetry takes place. In Mn_2BO_4 the CO appears to be related to the strong Jahn–Teller distortion of the $Mn1O_6$ octahedra. CO of the $Mn^{2+}(2)$–$Mn^{3+}(1)$–$Mn^{3+}(1)$–$Mn^{2+}(2)$ kind and relevant orbital ordering (d_z^2) occurs. From the magnetic point of view the Fe_2BO_4 was found to be a L-type ferrimagnet with the transition temperature $T_N = 155\ K$ [20]. As for the Mn_2BO_4, the situation is more intriguing. Nowadays this compound is known in three forms: single crystals [15], powder polycrystals [21–23], and necklace-like nanofibres [24]. The magnetic characterization has been carried out for the two first forms of Mn_2BO_4 and the results obtained are dramatically controversial. On one hand, magnetization, specific heat, and ESR studies of polycrystalline samples have revealed an antiferromagnetic transition at $T_N = 104\ K$ and weak ferromagnetism below 70 K. Recent neutron diffraction data have shown the occurrence of the long-range antiferromagnetic order only below 26 K [23], while the ferrimagnetic transition at 42 K was found from magnetization measurements. On the other hand, a weak anomaly at ∼25 K was observed from the magnetic susceptibility measurements performed on single crystals. The reason of this dramatic disagreement probably lies in the samples quality. The authors of [21–23] marked the presence of magnetic impurities in the form of Mn_2O_3 and Mn_3O_4 oxides.

Thus, there is no clear understanding of either the type of magnetic order or the temperature of magnetic phase transition in Mn_2BO_4. This paper reports first magnetization and specific heat measurements carried out on the Mn_2BO_4 single crystals. The experimental observation of magnetic phase transition at $T_N = 26\ K$ strongly supports the neutron diffraction results [23]. Long-range antiferromagnetic order occurs below T_N. The magnetic measurements performed for two directions of the applied field with respect to the crystalline c-axis allowed to reveal uniaxial anisotropy. Based on the superexchange interactions analysis the magnetic behavior is explained and possible spin configuration for the ordered state of Mn_2BO_4 is offered.

2. Experimental procedure

The solid state reaction method was found to give rise to difficulties in the preparing of pure samples [21–23]. The main synthetic problems relate to the existence of concurring phases with different crystal structures. This problem has been discussed in detail in the well known systematic work by Capponi [7], where it has been shown that attempts to grow oxyborates $Co^{2+}Ga^{3+}BO_4$, $Co^{2+}Cr^{3+}BO_4$, and $Co^{2+}Sc^{3+}BO_4$ with the warwickite structure have lead to concomitant ludwigite phases $Co_2^{2+}Ga^{3+}BO_5$, $Co_2^{2+}Cr^{3+}BO_5$, and $Co_2^{2+}Sc^{3+}BO_5$ respectively. Due to this reason the exact parameters of growing process are of great importance for the successful preparation of single-phase material. At present work these parameters were defined after some probe reactions and X-ray diffraction control.

The solution has been made by the step by step melting of B_2O_3 oxide (6.9 g), $Bi_2Mo_3O_{12}$ (51 g), Mn_2O_3 (17.7 g) and Na_2CO_3 (4.1 g) at $T_1 = 1100°\ C$ during 3 hours. Then the temperature was rapidly lowered to $T_2 = 970\ °C$ followed by a slow cooling at a rate of 4 °C a day. In two days the crucible was pulled out from the furnace and the solution was removed. Single crystals spontaneously formed on the walls of the crucible were rinsed with the aqueous nitric acid at room temperature. The crystals were in the form of black needles up to 12 mm long, and the cross sectional area was smaller than $1.0 \times 0.5\ mm^2$.

The room temperature X-ray diffraction measurements were carried out using an X-ray diffractometer SMART APEX II (MoKα radiation, CCD detector).

The magnetization in a field was measured using the hand-made vibrating samples magnetometer (VSM) at the International Laboratory of High Magnetic Fields and Low Temperatures (Wroclaw, Poland). The dc magnetization has been measured as function of the temperature and applied magnetic field up to 140 kOe. The temperature interval was 1.8–300 K. The measurements were carried out for two directions of the external magnetic field relative to the crystallographic c-axis, which coincides with the needle's axis. The holder contribution was subtracted from the integral signal and the corrections associated with form anisotropy were taken into account.

The specific heat measurements have been done by the relaxation method on commercial PPMS Quantum Design platform in Shared Facility Centre of Lebedev Physical Institute of RAS in the entire temperature interval $(T = 2–300\ K)$. The experimental error did not exceed 1% for all temperatures.

3. Experimental results

3.1. X-ray diffraction and normal coordinates calculation

In this section, we present some crystallographic data, which are relevant for the theoretical discussion below. The Mn_2BO_4 has a monoclinic unit cell ($P2_1/n$ space group), with the angle $\beta \approx 90.751°$ slightly different from 90° (Table 1). No impurity phases have been detected by means of X-ray diffraction. All parameters are in good agreement with those reported earlier [15,23]. The metal ions have two distinct positions labeled as 1 and 2, which are at the general $4e$ Wyckoff positions, oxygen atoms have four distinct positions and boron has only one position. The atomic coordinates, isotropic displacement parameters, selected bond lengths and angles are listed in the Supplemental materials (SM) Tables SM1–SM3 [25].

The $Mn1O_6$ octahedron is considerably smaller that the $Mn2O_6$ one as deduced from the average ⟨M–O⟩ bond length (2.065 instead 2.210 Å). The smaller ⟨M–O⟩ distances lead to an increasing oxidation state and can indicate that the Mn^{3+} ions prefer the $M1O_6$ octahedra, while Mn^{2+} occupies the $M2O_6$ ones. As it was expected, the shortest distances (less than 1.5 Å) are B–O inside the BO_3 triangle, which is the most tightly bound group in oxyborate structures.

The Mn^{2+} and Mn^{3+} distribution over the metallic sites can be studied by means of bond valences sums (BVS) calculation [26]. These empirical estimations predict atomic charges of 3.20/2.95 for Mn1 and 2.01/1.85 for Mn2, when bond valence parameters are related to Mn^{2+}/Mn^{3+}. So, there is a clear propensity of Mn^{3+} to occupy the site 1 with atomic charge 2.95, while for Mn^{2+} it is the site 2 with atomic charge 2.01. The obtained values are in agreement with the BVS calculation results reported by Norrestam [15] confirming that Mn_2BO_4 is a transition metal oxyborate with the explicit charge ordering. The BVS value for the boron atom was found to be 2.96 close to the formal valence 3+.

Both $Mn1O_6$ and $Mn2O_6$ octahedra are distorted. The distortions of the coordination octahedra can be described by the normal coordinates Q_α ($\alpha = 1, 2, \dots 3N-3$; N – number of ligands), which are linear combinations of the Cartesian coordinates of

Table 1
Crystal data and structure refinement of Mn_2BO_4.

Empirical formula	Mn_2BO_4
Formula weight (g mol^{-1})	184.69
Crystal system	Monoclinic
Space group	$P2_1/n$
Unit cell parameters (Å, deg)	
a	9.2934(5)
b	9.5413(5)
c	3.2475(2)
β	90.7510(10)
Unit cell volume (Å^3)	287.93(3)
Z	4
Calculated density (g cm^3)	4.26023
Radiation	MoKα
Wavelenght, λ (Å)	0.71073
Temperature (K)	296
Crystal shape	Needle (along c)
Abs. coefficient (mm^{-1})	8.581
F(000)	348
Θ range (deg)	3.06–34.00
Limiting indices	$-14 \leq h \leq 14$
	$-14 \leq k \leq 14$
	$-5 \leq l \leq 4$
Reflections collected	4701
Reflections independent	1157
Data / restraints / parameters	1157 / 0 / 65
Extinction coefficient	0.200(4)
GooF	1.173
Final R indices	
$R1$	0.0184
$wR2$	0.0422
R indeces (all data)	
$R1$	0.0199
$wR2$	0.0428

Table 2
The normal coordinates and ligand's displacement (Å) for metal ions in the M1O$_6$ and M2O$_6$ octahedral complexes. The R_0 is the M–O distance in the undistorted octahedron, that are accepted such in order to provide a zero value of Q_1. R_0 is 2.054 and 2.092 Å, for Mn1 and Mn2 respectively.

Normal coordinates	Mn1		Mn2	
	Normal coordinate	Displacement	Normal coordinate	Displacement
Q_2	−0.3937	−0.1968	0.0330	0.0165
Q_3	−0.2122	−0.0919	0.0828	0.0358
Q_4	−0.3347	−0.1674	−0.2095	−0.1048
Q_5	−0.2045	−0.1023	−0.4691	−0.2345
Q_6	−0.2612	−0.1306	−0.2403	−0.1201
Q_7	0.0828	0.0414	−0.0703	−0.0351
Q_8	0.1464	0.0732	−0.4739	−0.2369
Q_9	−0.0688	−0.0344	−0.2562	−0.1281
Q_{10}	−0.0485	−0.0343	−0.0556	−0.0393
Q_{11}	0.0835	0.0590	−0.2871	−0.2030
Q_{12}	−0.0225	−0.0159	−0.0565	−0.0399
Q_{13}	0	0	0	0
Q_{14}	−0.0284	−0.0142	0.0679	0.0339
Q_{15}	−0.0371	−0.0185	−0.1763	−0.0881

oxygen, and classified according to the irreducible representations of the coordination complex symmetry (Table 2), in terms of the O_h symmetry group (Table SM4 [25]). The Q_1 coordinate describes high-symmetry distortions like the breathing-mode. The other normal coordinates correspond to the low – symmetry distortions like the Jahn–Teller (JT) (Q_2 and Q_3) and trigonal (Q_4, Q_5, Q_6) ones. The Q_3 coordinate presents tetragonal octahedral distortion along the z–axis, whereas the Q_2 ones corresponds to the distortions

with rhombic symmetry. The observed JT distortion is a combination of the normal modes Q_1, Q_2, and Q_3. There are a larger axial elongation of the Mn1O$_6$ octahedron along the O1–Mn1–O3 axis with the average axial radii 2.325 Å and the compression of the other four Mn1–O bonds (the average planar radii is 1.935 Å), which suggests a d_z^2 orbital ordering at the Mn1 site as will be discussed below. In contrary, the bonds distribution in Mn2O$_6$ is so that two long bonds (O1, O4) and two medium bonds (O2, O3) are roughly coplanar with an average radius of 2.238 Å, while the two remaining short bonds (O2, O4) are axial with the average radii 2.155 Å (see Fig. SM1 and Table SM3 [25]). It can be noted that both normal coordinates Q_2, Q_3 are considerably prevailing for the M1 site, testifying the pronounced JT distortion of Mn1O$_6$ octahedron. The trigonal distortions are comparable for both types of the octahedra.

The electrical field gradient (EFG) generated by the oxygen octahedron on the metal sites M1 and M2 is a tensor $G_{\alpha\beta}$. The main component V_{zz} of the $G_{\alpha\beta}$ has been calculated, yielding values 0.42 and 0.11 e A^3 for Mn1 and Mn2 sites, respectively. Thereby, the Mn1O$_6$ octahedron was found to be ∼4 times more distorted than the Mn2O$_6$ one. The EFG principal axis lies along the M1–O1 (2.379 Å) and M2–O2 (2.088 Å) bonds. The EFG principal axes of Mn2–Mn1 pair are parallel and antiparallel to that of neighbor Mn1–Mn2 pair (Fig. SM1 [25]). This indicates the inversion of the principal axis in the ribbon substructure.

The main results of the structural study on Mn_2BO_4 may be written as follows: (i) the trivalent and divalent Mn ions occupy the M1 and M2 sites, respectively, that leads to the charge ordering in the row $Mn^{2+}(2)$–$Mn^{3+}(1)$–$Mn^{3+}(1)$–$Mn^{2+}(2)$; (ii) the Q_2 and Q_3 dominated modes corresponding to the JT distortions are significantly pronounced for Mn1O$_6$ octahedra; (iii) strong JT distortion of Mn1O$_6$ octahedra suggests a d_z^2 orbital at the Mn1 site; and (iv) there is an inversion center of the principal axis of octahedra at the center of the row.

3.2. dc Magnetization

Fig. 1(a) shows the magnetization curves as a functions of temperature, measured with the applied field perpendicular and parallel to the c-axis. It can be
seen that the homometallic manganese warwickite is an antiferromagnet with its easy axis of the magnetization perpendicular to the crystalline c-axis. Broad maxima near 30 K are pronounced. In the top inset the dependences of the derivative dM/dT as function of the temperature for both directions of the applied field are shown. From these curves we have obtained $T_N = 26$ K in agreement with the previous data [15,23]. In the bottom inset a zoom of the field-cooled (FC) and zero-field-cooled (ZFC) dc magnetization curves as a function of temperature for the applied field perpendicular to the c-axis are depicted. We note that no thermo-irreversibility between the FC and ZFC curves occurs below a critical temperature, that allows suggesting an antiferromagnetic long range spin arrangement in Mn_2BO_4.

Fig. 1(b) shows the linearization of the inverse dc susceptibility ($1/\chi_{dc}$). The Curie–Weiss law is obeyed within an extensive temperature range. The Curie–Weiss temperatures were found to be $\theta = -118$ K and -134 K for the applied field parallel and perpendicular to c-axis, respectively. The θ temperatures are negative, strongly supporting that the antiferromagnetic interactions as dominant. We note that this result is contrary to the reported data [22], where the positive value of Curie–Weiss temperature has been found. The ratio $\frac{\theta}{T_N} \approx 5$ indicates the presence of disordering components in the magnetic coupling network. The effective magnetic moments per formula unit obtained from Curie–Weiss constants
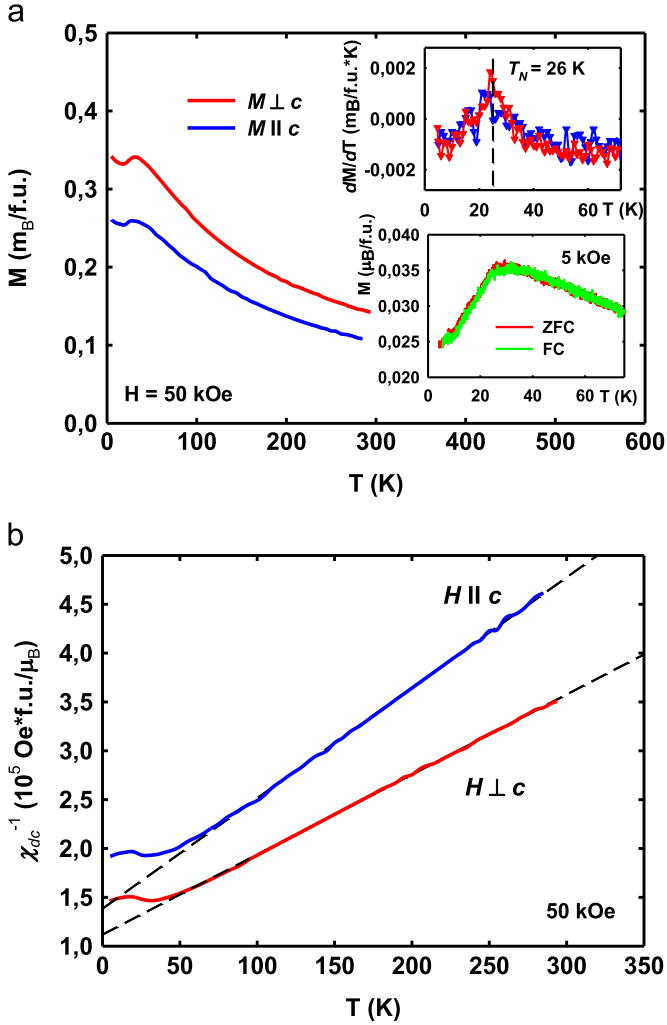
a

b

Fig.. 1 (a) The temperature dependencies of *dc* magnetization of Mn_2BO_4 single crystal measured in applied field of 50 kOe directed along two orthogonal directions: parallel (H∥) and perpendicular (H⊥) *c*-axis. The top inset shows the peak of the derivative *dM/dT* corresponding to the critical temperature T_N. The bottom inset is the field-cooled and zero-field-cooled magnetization curves measured for the applied field perpendicular to the *c*-axis. (b) The inverse susceptibility as a function of the temperature at *H*=50 kOe.

were found to be 6.25 and 6.95 μ_B for the parallel and perpendicular directions of the applied field, respectively. Assuming that both Mn ions are in the high-spin state we calculated the spin component of the effective moment neglecting the orbital component. Accounting for the contribution of each type of Mn ions, the spin component is given by $\mu_s^2 = \sum_i g_i^2 S_i(S_i + 1)$. The effective moment per formula unit with one divalent (*S*=5/2) and one trivalent (*S*=2) Mn ions and *g*=2 is $\mu_S = 7.68\ \mu_B$. This value is larger than that experimentally found. The effective magnetic moment per formula unit taking into account the orbital contribution is expressed by $\mu_J^2 = \sum_i g_i^2 J_i(J_i + 1)$. We have estimated the value of μ_J using the results of Ref. 27, where the orbital magnetism has been taken into account in the description of electron level energies in the 3d-ion compounds. For Mn^{3+} ion (d^4) *J*=1 and *g*=1.1, and for Mn^{2+} ion (d^5) it is *J*=5/2 and *g*=2. The obtained value is μ_J=6.12 μ_B. The result assumes that the orbital moments of Mn^{3+} ions are not quenched and contribute to the observed magnetic moment. This result also supports the neutron diffraction data [23], showing the considerably reduced Mn^{3+} magnetic moments μ=1.0 μ_B.

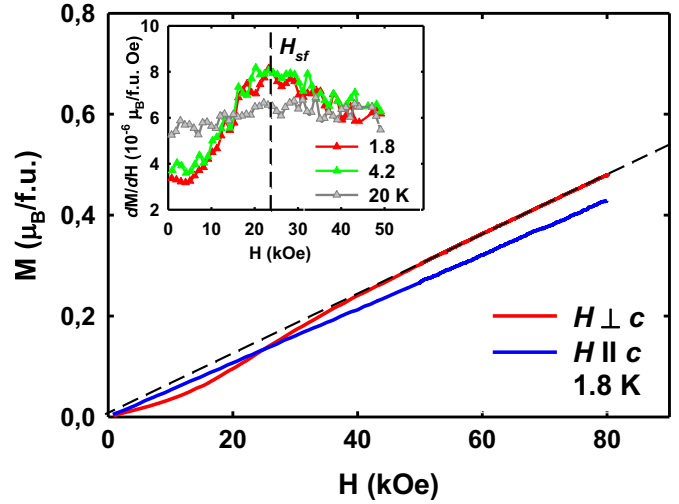Magnetization as a function of applied magnetic field was

Fig. 2. The field dependences of Mn_2BO_4 magnetization for two orthogonal directions of the.

measured in the temperature range 1.8–75 K for both directions of external field. We note that the curves do not display the saturation up to 140 kOe. The isotherms of magnetization at 1.8 K vs applies field are plotted in Fig.2. The magnetization isotherm measured with applied field perpendicular to *c*-axis shows the inflection point at the field H_{sf}=24 kOe, which can be determined as the maxima in the derivative function plotted in the coordinates of *dM/dH* vs *H* (top inset). The derivatives of the isotherms measured at 4.2 and 20 K are also displayed. As the temperature increases the curve becomes smooth, nevertheless, the transition can be observed right up to 20 K. We identified the critical field corresponding to the maxima as a spin-flop field.

The magnetization isotherms measured for the applied field parallel to *c*-axis do not show any peculiarities, pointing out that the easy axis of magnetization lies in the ab plane, which confirms the results of the magnetization measurements as a function of temperature.

3.3. Specific heat

Further evidence for AF transition is obtained from the specific heat data. The specific heat measurement data at *H*=0 are shown in Fig. 3(a), where the specific-heat curve is plotted in the coordinates *C/T* versus *T*. One can clearly see a peak at the magnetic ordering temperature T_N^*=23 K. We note that the specific heat magnitude of Mn_2BO_4 is higher than those of $MgScBO_4$ in wide temperature range [22], which has no magnetic contribution to the specific heat. Our attempts to fit the low-temperature data range by the power law $C/T = \gamma + \beta T^2$ have yielded the following fitting parameters: γ=2.52 mJ/mol K² and β=9.54 mJ/mol K⁴. The linear term turns out to be of the same order of magnitude as for the related ludwigites Co_3BO_5 and Co_2FeBO_5 (3.30 and 3.28 mJ/mol K², respectively) [28]. Note that our attempts to measure the transport properties of Mn_2BO_4 single crystal have not been successful due to extremely large resistance of the sample ($> 10^8\ \Omega$ at room temperature). Taking into account the insulating nature of all mentioncompounds the question about the origin of this term remains open. The βT^3 is the contribution due to three-dimensional phonons in the Debye model. The application of this simplified model for the description of the low-temperature data of the specific heat gets too low value of effective Debye temperature than that expected for an oxyborate rigite structure. So, for correct description of the critical behavior of the specific heat and for an
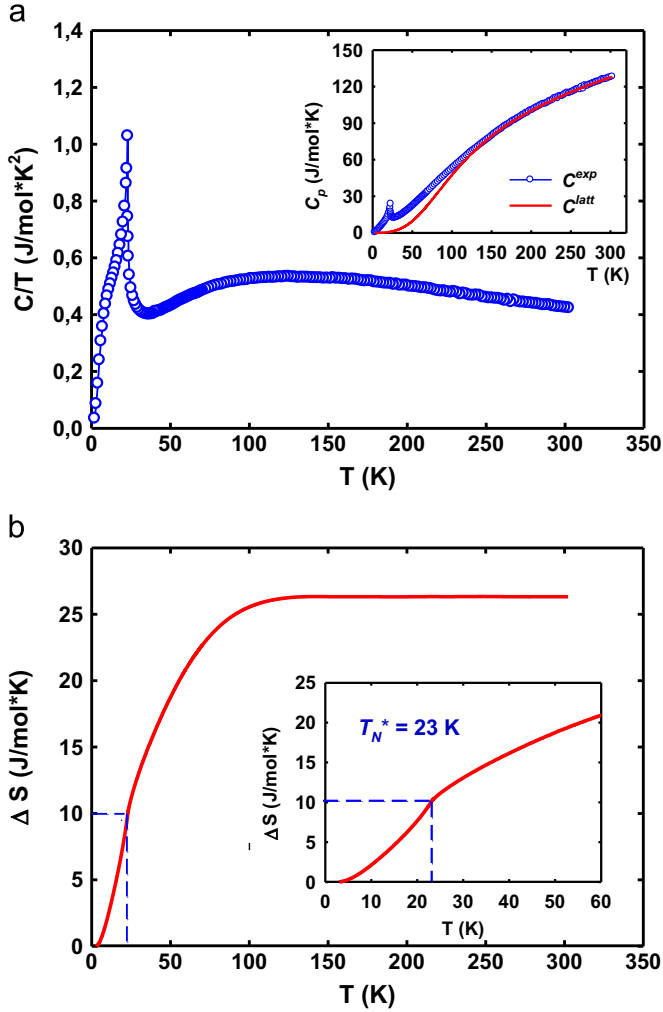
a

b

Fig. 3. (a) Specific heat of Mn_2BO_4 plotted as C/T versus T. The inset: experimental specific heat (blue circle) and the lattice contribution to the specific heat obtained by fitting to Eq. (2) (red solid line). (b) Entropy as a function of temperature. The inset: the zoom of the magnetic transition range, S (T_N)=10.06 J/mol K. (For interpretation of the references to color in this figure legend, the reader is referred to the web version of this article.)

anomalous part separation, it is necessary to consider other contributions to the specific heat.

The specific heat of a crystalline solid can be expressed by the sum of three main contributions

$$C_V = C_V^{latt} + C_V^{mag} + C_V^{Sch} \tag{1}$$

where C_V^{latt} is the lattice vibration contribution, C_V^{mag} is the magnetic contribution, and C_V^{Sch} is the Schottky contribution. The crystal defects, anharmonicity effect, and free electrons contributions are small and can be neglected. The difference between C_V and C_p can be evaluated by the thermodynamic relationship, which requires knowledge of thermal expansion coefficient, material's volume, and isothermal compressibility. However, the difference between C_V and C_p was shown to be important only at high temperatures [29]. In order to quantitatively estimate the critical behavior near T_N the anomalous contribution of the specific heat $\Delta C_V = C_V^{mag} + C_V^{Sch}$ was separated from the measured dependence of the specific heat by subtracting of the regular lattice contribution C_V^{latt}. The latter can be expressed using simple model including Debye and Einstein approximations. The lattice contribution to the specific heat is given by the equation:

$$C_V^{latt}/R = K_D D(\Theta_D/T) + K_E E(\Theta_E/T) \tag{2}$$

whereand

$$D(\Theta_D/T) = 9\frac{1}{(\Theta_D/T)^3}\int_0^{\Theta_D/T}\frac{(\Theta_D/T)^4 exp(\Theta_D/T)}{[exp(\Theta_D/T) - 1]^2}d(\Theta_D/T),$$

$$E(\Theta_E/T) = 3(\Theta_E/T)^2\frac{exp(\Theta_E/T)}{[exp(\Theta_E/T) - 1]^2}$$

and shown in the inset Fig.3a. Here, R is the gas constant, Θ_D, Θ_E is characteristic Debay and Einstein temperatures, the K_D, K_E are numerical coefficients. The fit in the temperature range $T > 130$ K gives follow estimations of parameters $\Theta_E = 695$ K, $\Theta_D = 299$ K. The obtained value of Θ_D is well agreed with that for $MgScBO_4$ ($\Theta_D = 306$ K).

The non-lattice contribution to the entropy (ΔS) including the magnetic (ΔS_{mag}) and Schottky (ΔS_{Sch}) entropies is presented in Fig.3b. The full magnetic ordering should accompanied by the entropy released of $\Delta S_{mag} = R[\ln(2S1 + 1) + \ln(2S2 + 1)]=28.278$ J/mol K expected for one Mn^{3+} ($S1=2$) and one Mn^{2+} ($S2=5/2$) ions per formula unit. The entropy at the critical temperature is ΔS (T_N)=10.06 J/mol K, that is less than half of the theoretical limit of magnetic entropy ΔS_{mag}. Thus, at the temperatures well above T_N the magnetic entropy is associated with the retention of short-range magnetic order in the magnetic spin system. As the temperature increases the magnetic correlations vanish. This fact is consistent with the magnetization data and theoretical calculation of the superexchange interactions.

4. Uniaxial anisotropy and exchange interactions

The experimental data have shown that Mn_2BO_4 can be considered as standard uniaxial antiferromagnet with easy axis of magnetization lied at the crystallographic ab plane. We have estimated the anisotropy constant K and anisotropy field H_a values in Mn_2BO_4

$$K(T) = \frac{1}{2}H_{sf}^2(\chi_\perp - \chi_\parallel)$$

$$H_a = \frac{K}{M_s} \tag{3}$$

where $\chi_\perp$ and $\chi_\parallel$ are the experimental values of magnetic susceptibilities above and below critical field H_{sf}, M_s is the sublattice magnetization. Assuming that the average spin per formula unit is $S = \frac{1}{n}\sum_{i=1}^n S_i = 2.25$, where n denotes the number of magnetic ions per formula unit, the obtained value is $K(1.8$ K$)=48.03$ erg/cm^3, which corresponds to $H_a=165$ Oe. These values are in a good agreement with that reported earlier for $Mn_2B_2O_5$ pyroborate, where only one type of manganese ion is present [30]. The exchange field acting along the crystalline c-axis was found to be $H_{ex\parallel}=834$ kOe, while the exchange field inside the ab-plane is $H_{ex\perp}=766$ kOe.

In a molecular field approximation for a two-sublattice model with one exchange interaction J, the exchange parameter and the Neel temperature are related by simple expression

$$z|J| = \frac{3k_B}{2S(S + 1)}T_N \tag{4}$$

where z is the number of nearest neighbors with the exchange interaction J, k_B is the Boltzmann constant. Putting the values of $T_N=26$ K and average spin, we get $z|J|= 5.33$ K.

A consistent approach to analyze of the magnetic behavior of

Mn$_2$BO$_4$ requires calculating the superexchange interaction. We note that the estimations of the superexchange interactions have been made earlier in the work [23], but the interaction through t_{2g}-orbits wasn't taken into account, along with the interribbon interactions. We present a deep analysis of superexchange interaction in Mn$_2$BO$_4$, considering all nonequivalent superexchange pathways of ferromagnetic and antiferromagnetic nature. It has allowed to explain the observed magnetic behavior and to offer a scenario of the magnetic ordering in Mn$_2$BO$_4$.

The inter-ion distances inside the ribbon are of the order of 3 Å as can be seen from the crystallographic data. Namely, the shortest is Mn^{3+}–Mn^{3+} (2.84 Å), and the longest is Mn^{2+}–Mn^{3+} (3.36 Å). That is too long for a direct orbital overlap. The anisotropy energy is much smaller than the exchange one ($\sim$0.25 K versus $\sim$5 K). We have used the simple model of superexchange interactions [31] applied earlier to the analysis of the complex magnetic structure in Co$_3$O$_2$BO$_3$, Co$_2$FeO$_2$BO$_3$ ludwigites [1,5], and Co$_3$B$_2$O$_6$ kotoites [32], which offered satisfactory agreement with the experimental results. Manganese warwickite Mn$_2$BO$_4$ belongs to the related family of oxyborates that justifies the analogous study. The calculation is restricted by the nearest-neighbor approximation; i.e. only the interactions along the short M–O–M bonds are considered, while the long bonds M–O–M–O–M and M–O–B–O–M are neglected. The ferromagnetic (F) and antiferromagnetic (AF) contributions to Mn–O–Mn couplings exist. Orbitally non-generate Mn^{2+} states (d^5) have singly occupied e_g orbitals, that supposes the antiferromagnetic exchange interaction to be dominant. The Mn^{3+} states (d^4) have one e_g hole at d_{x2-y2} orbital, that leads to ferromagnetic (F) contributions to the exchange integrals.

The Mn$_2$BO$_4$ warwickite structure has several types of indirect couplings: 92°, 95–99°, 102°, and 105°, which can be assigned to 90° exchange interactions, as well as 115°, 119° and 125° exchange interactions. In the 2–1–1–2 row the neighboring cations with common octahedral edges take part in the exchange couplings with bond angles of 99–105° ($J1$) and 97° ($J2$). The octahedra belonging to the adjacent rows, which are connected by a common edge, allow indirect couplings 92–105° ($J3$), 96–102° ($J4$), 95° ($J5$), and 89–102° ($J6$). The octahedra connected by a common oxygen ion and belonging to the adjacent ribbons allow indirect couplings of 115°, 119°, and 125°, corresponding to $J7$, $J8$, and $J9$ exchange interactions respectively. So, the magnetic structure of Mn$_2$BO$_4$ can be described by nine exchange integrals $J1$–$J9$, where $J1$–$J6$ are intra-ribbon interactions, while $J7$–$J9$ are inter-ribbon ones. The full set of orbitals pairs participating in the coupling is presented in Table SM5 [25]. The total integral of cation–cation exchange interaction J can be calculated as a sum of individual orbital exchange integrals

$$J = \frac{1}{4} \sum_{i,j=1}^{5(d)} \sum_{p=1}^{3} \frac{1}{S_i S_j} I_{ij}^p \tag{5}$$

where S_i-and S_j are the interacting cations spins; the sum accounts for the five magnetic ion d-orbitals and three p-orbitals of the ligand; I_{ij}^p– the superexchange interaction integral between the individual orbitals i, j of two cations via oxygen p orbital. Interactions between two filled or two empty orbitals are neglected.

Taking into account superexchange bonds selected by lattice symmetry and cation distribution we have written the expressions for the exchange integrals as follows:

$$J1 = -\frac{1}{20}c\left[\left(\frac{10}{3}b + 2c\right)(U_1 + U_2) - 2bJ_{in}\right] = -4.03K$$

$$J2 = -\frac{1}{16}c\left[\left(\frac{4}{3}b + 2c\right)(U_1 + U_2) - 4bJ_{in}\right] = -1.44K$$

$$J3 = -\frac{1}{16}c\left[\left(\frac{13}{3}b + 2c\right)(U_1 + U_2) - bJ_{in}\right] = -6.83K$$

$$J4 = -\frac{1}{16}c\left[\left(\frac{10}{3}b + 2c\right)(U_1 + U_2) - 2bJ_{in}\right] = -5.03K$$

$$J5 = J4$$

$$J6 = -\frac{1}{25}c\left(\frac{16}{3}b + 4c\right)(U_1 + U_2) = -5.21K$$

$$J7 = -\frac{1}{20}\left(\frac{16}{9}b^2 + 2c^2\right)(U_1 + U_2)|\cos119°| = -2.41K$$

$$J8 = -\frac{1}{20}\left[\left(\frac{4}{9}b^2 + 2c^2\right)(U_1 + U_2) - \frac{4b^2}{3}J_{in}\right]|\cos115°|$$
$$= -0.47K$$

$$J9 = -\frac{1}{20}\left[\left(\frac{4}{9}b^2 + 2c^2\right)(U_1 + U_2) - \frac{4b^2}{3}J_{in}\right]|\cos125°|$$
$$= -0.65K \tag{6}$$

The factor $|\cos\theta|$ accounts for the angle dependence of the transfer parameters. The basic parameters of the model are the ligand–cation excitation energies U ($U_1 = U(Mn^{3+}–O) = 5.0$ eV, $U_2 = U(Mn^{2+}–O) = 4.4$ eV), intra-atomic exchange energy J_{in} ($J_{Mn^{3+}} = 3.0$ eV) and electron transfer parameters $b = 0.02$ (σ-coupling), $c = 0.01$ (π-coupling) defined in theRef. [33]. The calculated values are presented also. The integrals $J5 = J4$ are equivalent because the similar magnetic ions interact through the same electron orbitals. One can note that the exchange integral values are comparable with those $z|J|$ estimated from the T_N, assuming $z = 1$. The intraribbon interactions ($J1$–$J6$) are comparative in magnitude and considerably exceed the interribbon ones. The AF intra-row interaction $J2$ is quenched by ferromagnetic pathway from the $e_g$hole on d_{x2-y2} orbitals of Mn^{3+} ions. The $J6$ interaction includes antiferromagnetic superexchange pathways only due to singly occupied five d-orbitals of Mn^{2+}.

To gain insight into the magnetic properties of Mn$_2$BO$_4$ the division into magnetic sublattices is needed. The number of magnetic sublattices is determined by the different cations number, nonequivalent local cation positions number relative to the principal crystal axes, and interaction sign between the nearest neighbors at last. In Mn$_2$BO$_4$ the octahedra principal axes have four different directions relative to the cell axes (Fig. SM1). Let warwickite be considered as a magnetic system consisting of eight magnetic sublattices in which crystallographic positions M1 and M2 are divided into four magnetic sublattices: 1a, 1b, 1c, 1d and 2a, 2b, 2c, 2d, that leads to two types of the rows 2a-1a-1b-2b and 2c-1c-1d-2d (Fig. 4).

The exchange interaction parameters calculated taking into account the nearest neighbors numbers (z_{ij}) are collected in Table 3. The mutual orientation of the sublattices magnetic moments is shown by arrows. The exchange integrals of minimum energy correspond to the strongest coupling. As can be seen, the strongest interactions are $2 \cdot J4$ and $2 \cdot J6$ (via two equivalent pathways, $z_{ij} = 2$) between the manganese ions belonging to the chains 1a–1c–1a, 1b–1d–1b, 2a–2c–2a, 2b–2d–2b extending along c-axis.

The strong inter-chain interaction $|J3| = 6.83$ K favors antiferromagnetic alignment of Mn^{2+} and Mn^{3+} moments. These three interactions reinforce each other and impose the antiferromagnetic alignment between the magnetic moments of 1a sublattice and those of 1c, 2c sublattices. The same interactions lead to the magnetic moments of the 1b sublattice to be ordered

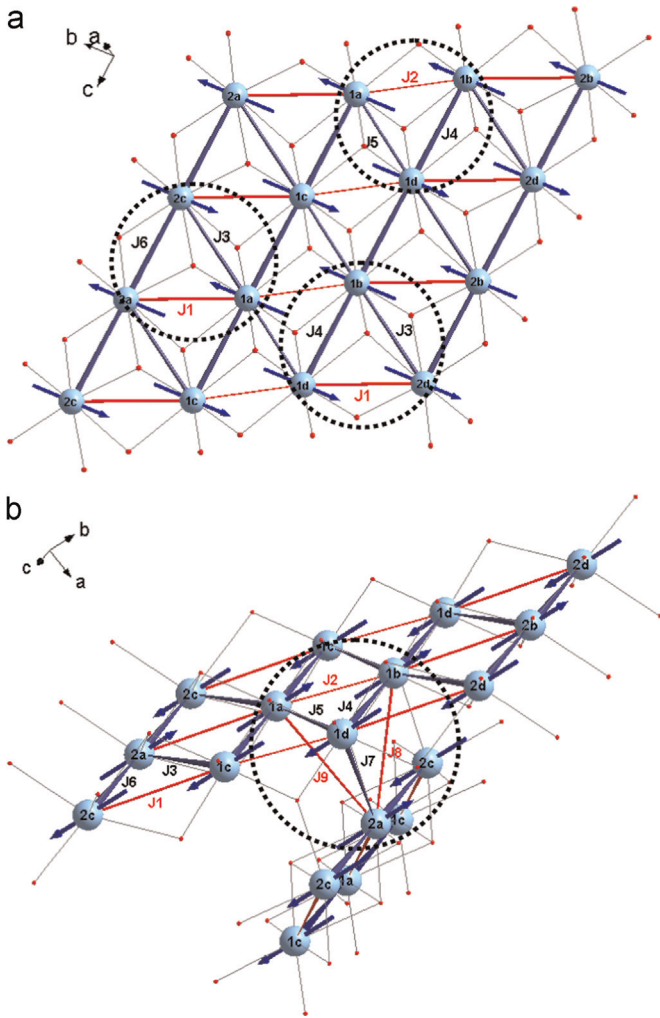**Fig. 4.** (a) the intra-ribbon indirect exchange interactions (*J1–J6*) and (b) inter-ribbon ones (*J7–J9*) in the Mn_2BO_4 warwickite. Numerals indicate the belonging of a crystallographic position to a magnetic sublattice. The frustrated bonds are highlighted red. The interactions strength is shown by the lines thickness. The magnetic moments direction is randomly chosen at the crystallographic ab-plane and demonstrates the ordering and disordering bonds. The non-equilateral triangles are highlighted by the circles.

denoted in italic in Table 3 and with red lines in Fig. 4.

In a molecular field approximation for the multisublattice model the exchange field operating on magnetic ions with spin S_i, belonging to *i*-th sublattice caused by other sublattices is given by the expression

$$H_{exi} = \sum_{j=1}^{p} \frac{2J_{ij}}{g_i g_j \mu_B^2} \mu_j \tag{7}$$

$$\mu_j = g_j \mu_B S_j$$

Here *i, j = 1, 2, …, p* denote sublattice numbers (*p=8* at present case), J_{ij} is the exchange interaction parameter between the sublattices, g_i, g_j are spectroscopic factors, μ_B- Bohr magneton, and S_j is spin of the magnetic ion belonging to *j*-th sublattice. In Mn_2BO_4 the exchange fields acting on the magnetic ions are defined by the competition between ordering and disordering interactions. We have estimated the exchange fields H_{exi} acting on the manganese ions belonging to the 1 *a*-1*d* and 2 *a*-2*d* sublattices and obtained the values of $H_{ex}^{1a-1d}=558$ and $H_{ex}^{2a-2d}=509$ kOe, respectively. These values are well agreed with those obtained from *dc* magnetization measurements.

5. Discussion

This work presents a careful study of the magnetic properties of homometallic manganese warwickite through *dc* magnetization and specific heat measurements. Magnetic characterization is supported with XRD analysis and superexchange interactions calculations. The X-ray data analysis and normal coordinates calculation have shown that Mn_2BO_4 demonstrates the charge ordering of $Mn^{2+}(2)$-$Mn^{3+}(1)$–$Mn^{3+}(1)$–$Mn^{2+}(2)$. The JT distortions result in the compression of the $Mn2O_6$ and the considerable elongation of $Mn1O_6$ octahedra along one of the nominal 4-fold axis. The latter suggests a d_{z^2} orbital at the Mn1 site.

The magnetization measurements have been carried out for two directions of the applied magnetic field: parallel and perpendicular to the crystalline *c*-axis. A small anisotropy is observed between two directions of the magnetic field. Our magnetic studies have clearly revealed the anomaly in the behavior of *dc* magnetization at $T_N=26$ K which can be unequivocally identified as long-range antiferromagnetic transition. The results of the specific heat strongly support the above-mentioned suggestion, where the λ-type anomaly was found at $T_N^*=23$ K, indicating a second-order phase transition. At temperatures $T_N^* < T < 125$ K the short-range magnetic correlations develop, leading to the decrease in the entropy ΔS and high values of Curie–Weiss temperatures. The easy axis of the magnetization lies in the ab-plane and spin-flop transition takes place at $H_{sf}=24$ kOe. The low uniaxial anisotropy H_a is probably associated with orbitally non-degenerate Mn^{2+} state (*S* state). According to the neutron diffraction data the $Mn^{2+}(2)$ moments are parallel to *b*-axis [23]. One can conjecture that the spin-flop

antiferromagnetically with respect to those of 1*d* and 2*d*. This type of coupling is marked as "ordering interaction" and denoted in bold in Table 3, and with bold lines in Fig. 4, where the calculated local magnetic structure, depicting the short range order, is presented. According to these ordering interactions the arrows directions (↑ or ↓) have been established. The relative weak *J1, J2, J8* and *J9* interactions tend to disturb the AF order imposed by dominant ordering interactions. Such couplings have frustrating character and are named as "disordering interactions". They are

Table 3
The exchange interactions integrals (K) in Mn_2BO_4 warwickite. The strongest ordering interactions are shown in bold. The disordering interactions are shown in italic.

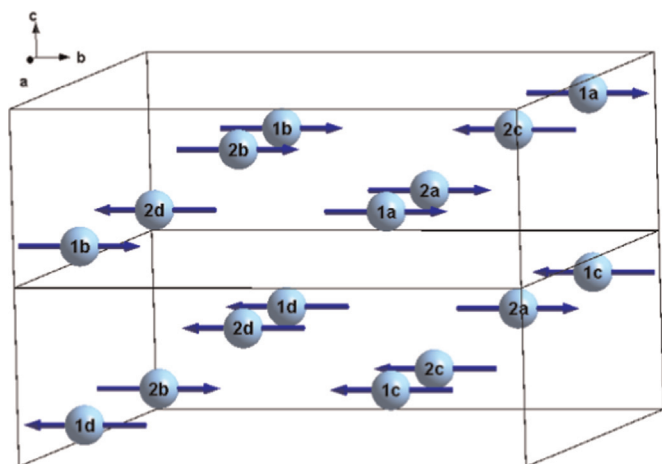|	1a ↑	1b ↑	1c ↓	1d ↓	2a ↑	2b ↑	2c ↓	2d ↓
1a ↑	0	*− 1.44*	**− 10.06**	**− 5.03**	− 4.68	− 0.47	**− 6.83**	− 2.41
1b ↑	*− 1.44*	0	**− 5.03**	**− 10.06**	− 0.47	− 4.68	− 2.41	**− 6.83**
1c ↓	**− 10.06**	**− 5.03**	0	*− 1.44*	**− 6.83**	− 2.41	− 4.68	− 0.47
1d ↓	**− 5.03**	**− 10.06**	*− 1.44*	0	− 2.41	**− 6.83**	− 0.47	− 4.68
2a ↑	− 4.68	− 0.47	**− 6.83**	− 2.41	0		**− 10.42**	
2b ↑	− 0.47	− 4.68	− 2.41	**− 6.83**		0		**− 10.42**
2c ↓	**− 6.83**	− 2.41	− 4.68	− 0.47	**− 10.42**		0	
2d ↓	− 2.41	**− 6.83**	− 0.47	− 4.68		**− 10.42**		0

Fig. 5. The spin configuration for the ordered state of Mn_2BO_4 warwickite resulting from the simple model of superexchange interactions. The double magnetic unit cell along c-axis is shown.

transition at H_{sf} is due to the flopping of the magnetic moments of Mn2-Mn2 inside the antiferromagnetic chain. The effective magnetic moments values 6.25 and 6.95 μ_B/f.u. obtained for two orthogonal directions of the external magnetic field may be the result of the non-quenched orbital moment of Mn^{3+} ions, as well as the intraribbon frustrating superexchange interactions.

The geometric frustrations are underlying by the warwickite structure. There is almost hexagonal arrangement of Mn ions inside the ribbon. The several types of triangular motifs both inside the ribbon and between the adjacent ribbons exist (see Fig. 4 and Table SM3 [25]). Three triangles are resolved inside of the ribbon involving different exchange couplings $J1$–$J3$–$J6$, $J1$–$J3$–$J4$ and $J2$–$J4$–$J5$. The disordering coupling $|J2| = 1.44$ K is weak in comparison with $|J4| = |J5| = 5.03$ K and does not break the FM alignment of moments within the row 2–1–1–2. While the rather strong AF coupling $|J1| = 4.03$ K favors an AF alignment of moments Mn^{2+}–Mn^{3+} within the row, it leads to considerable frustration of the intra-chains interactions along c-axis. The geometry of interribbon bonds such that three types of triangles can be singled out also: $J4$–$J7$–$J8$, $J2$–$J8$–$J9$, and $J5$–$J7$–$J9$. The rather weak interribbon couplings $|J8| = 0.47$ K and $|J9| = 0.65$ K are outweighed by strong $|J7| = 2.41$ K one. So, interribbon interaction $J7$ favors the AF alignment of magnetic moments $Mn^{2+}(2)$ and $Mn^{3+}(1)$ belonging to adjacent ribbons and can be responsible for long-range order in Mn_2BO_4. The magnetic frustration experimentally manifests itself in the large ratio of $|\theta|/T_{C,N}$, which is considered as the frustration criteria [34]. For instance, for ferromagnetic materials $|\theta|/T_C \sim 1$, for antiferromagnetic systems, $|\theta|/T_N \sim 2$–5. For the majority of the warwickites of interest the value $|\theta|/T_{SG}$ ranges from 8 to 37, which is consistent with a high level of frustration [6,8,10]. The value of $|\theta|/T_{SG}$ was found to be ~ 5 in Mn_2BO_4. We conclude, that in spite of the magnetic frustration is present in Mn_2BO_4 no dramatic frustration level occurs, allowing the on-set of long magnetic order at $T_N = 26$ K. In spite of the simplicity of the theoretical method, the calculations have been shown to provide a correct description of the magnetic behavior of Mn_2BO_4. Therefore, it could be considered as an available tool for basic and qualitative understanding of magnetic properties of warwickites and related oxyborates.

In summary, homometallic warwickite Mn_2BO_4 can be considered as a conventional antiferromagnet showing uniaxial anisotropy. The long-range order occurs below $T_N = 26$ K. The dominant exchange interaction is antiferromagnetic as was found from the superexchange interactions calculations. The strongest interactions are the intra-ribbon ones between the cations along c-axis ($J4$ and $J6$). As a result, antiferromagnetic chains $2a$–$2c$–$2a$, $1a$–$1c$–

$1a$, $1b$–$1d$–$1b$, and $2b$–$2d$–$2b$ extending along c-axis occur. (ii) It leads to the doubling of the magnetic cell along the c-axis (Fig. 5). We note that a magnetic supercell with twice the volume of the structural cell was found in Mn_2BO_4 by neutron diffraction measurements [23], but the doubling direction was not defined. (iii) The magnetic coupling between two adjacent ribbons is depressed due to frustrating interactions $J8$, $J9$. The three-dimensional AF ordering is supported by the inter-ribbon interaction $J7$ via the coupling Mn^{3+}–O–Mn^{2+} with the coupling angle 115°, where Mn^{3+} and Mn^{2+} ions belong to the adjacent ribbons.

Supporting Information available

Structure parameters, refined bond lengths and angles according to Reitveld refinements of the XRD data, the normal coordinates expressed in Cartesian shifts, the tabulated parameters for superexchange interactions calculation in Mn_2BO_4.

Appendix A. Supplementary material

Supplementary data associated with this article can be found in the online version at http://dx.doi.org/10.1016/j.jmmm.2015.05.081.

References

[1] J. Bartolome, A. Arauzo, N.V. Kazak, N.V.N.B. Ivanova, S.G. Ovchinnikov, Yu. V. Knyazev, I.S. Lyubutin, Phys. Rev. B 83 (2011) 1–12 144426.
[2] H. Yamane, T. Kawano, J. Cryst. Soc. Jpn. 54 (2012) 68–73.
[3] D.C. Freitas, R.B. Guimaraes, J.C. Fernandes, M.A. Continentino, C.B. Pinheiro, J. A.L.C. Resende, G.G. Eslava, L. Ghivelder, Phys. Rev. B 81 (2010) 1–7 174403.
[4] Yu.V. Knyazev, N.B. Ivanova, N.V. Kazak, M.S. Platunov, L.N. Bezmaternykh, D. A Velikanov, D. Vasiliev, S.G. Ovchinnikov, G.Yu Yurkin, J. Magn. Magn. Mater. 324 (2012) 923–927.
[5] N.V. Kazak, N.B. Ivanova, O.A. Bayukov, S.G. Ovchinnokov, A.D. Vasiliev, V. V. Rudenko, J. Bartolome, A. Arauso, Yu.V. Knyazev, J. Magn. Magn. Mater. 323 (2011) 521–527.
[6] A. Apostolov, M. Mikhov, P. Tcholakov, Phys. Status Solidi A 56 (1979) K33–K36.
[7] J.J. Capponi, J. Chenavas, J.C. Joubert, J. Solid State Chem. 7 (1973) 49–54.
[8] M.A. Continentino, B. Boechat, R.B. Guimãraes, J.C. Fernandes, L. Ghivelder, J. Magn. Magn. Mater. 226–230 (2001) 427–430.
[9] R.B. Guimãraes, J.C. Fernandes, M.A. Continentino, H.A. Borges, C.S. Moura, J.B. M. da Cunha, C.A. dos Santos, Phys. Rev. B 56 (1997) 292–299.
[10] A. Arauzo, N.V. Kazak, N.B. Ivanova, M.S. Platunov, Yu.V. Knyazev, O. A. Bayukov, L.N. Bezmaternykh, I.S. Lyubutin, K.V. Frolov, S.G. Ovchinnikov, J. Bartolomé, J. Magn. Magn. Mater. 642 (2015) 204–209.
[11] N.V. Kazak, M.S. Platunov, N.B. Ivanova, Y.V. Zubavichus, A.A. Veligzhanin, A.D. Vasiliev, L.N. Bezmaternykh, O.A. Bayukov, A. Arauzo, K.V. Lamonova, S.G. Ovchinnikov, Phys. Status Solidi B. arXiv:1412.6236 (2015) (submitted for publication).
[12] I.S. Lyubutin, N.Y. Korotkov, K.V. Frolov, N.V. Kazak, M.S. Platunov, Y. V. Knyazev, L.N. Bezmaternykh, J. Alloy. Compd. 642 (2015) 204–209, http://dx.doi.org/10.1016/j.jallcom.2015.04.067.
[13] Yu. V. Knyazev, N.V. Kazak, M.S. Platunov, N.B. Ivanova, L.N. Bezmaternykh, A. Arauzo, S.G. Ovchinnikov, J. Alloy. Compd. 642 (2015) 232–237, http://dx.doi.org/10.1016/j.jallcom.2015.04.056.
[14] J.P. Attfield, A.M.T. Bell, L.M. Rodriguez-Martinez, J.M. Greneche, R.J. Cernik,

J.F. Clarke, D.A. Perkins, Nature 396 (1998) 655–658.

[15] R. Norrestam, M. Kritikos, A. Sjdin, J. Solid State Chem. 114 (1995) 311–316.
[16] A. Akrap, M. Angst, P. Khalifah, D. Mandrus, B.C. Sales, L. Forró, Phys. Rev. B 82 (2010) 1651061–1651067.
[17] G.R. Hearne, W.N. Sibanda, E. Carleschi, V. Pischedda, J.P. Attfield, Phys. Rev. B 86 (2012) 1951341–1951345.
[18] H.X. Yang, H.F. Tian, Y.J. Song, Y.B. Qin, Y.G. Zhao, C. Ma, J.Q. Li, Phys. Rev. Lett. 106 (2011) 0164061–0164064.
[19] Z. Chen, C. Ma, Y.J. Song, H.X. Yang, H.F. Tian, J.Q. Li, Phys. Rev. B 86 (2012) 0451111–0451116.
[20] J.P. Attfield, A.M.T. Bell, L.M. Rodrigues-Martinez, J.M. Greneche, R. Retoux, M. Leblanc, R.J. Cernic, J.F. Clarce, D.A. Perkins, J. Mater. Chem. 9 (1999) 205–209.
[21] B. Rivas-Murias, F. Rivadulla, M. Sanchez-Andujar, A. Castro-Couserio, M. A. Senaris-Rodrigues, J. Rivas, Chem. Mater 18 (2006) 4547–4552.
[22] M.A. Continentino, A.M. Pedreira, R.B. Guimaraes, M. Mir, J.C. Fernandes, R. S. Freitas, L. Ghivelder, Phys. Rev. B 64 (2001) 0144061–0144066.
[23] R.J. Goff, A.J. Williams, J.P. Attfield, Phys. Rev. B 70 (2004) 0144261–0144265.
[24] Sh. Li, J. Leng, Y. Fan, Ch. Fu, H. Shen, Y. Xue, D. Xu, Phys. Status Solidi A 208 (2011) 114–117.
[25] Supplementary Material for: Uniaxial anisropy and low-temperature anti-ferromagnetism of Mn2BO4 single crystal.
[26] I.D. Brown, D. Altermatt, Acta Cryst. B 41 (1985) 244–247.
[27] R.J. Radwanski, Z. Ropka, Acta Phys. 1 (2006) 3–11.
[28] D.C. Freitas, M.A. Continentino, R.B. Guimarães, J.C. Fernandes, E.P. Oliveira, R. E. Santelli, J. Ellena, G.G. Eslava, L. Ghivelder, Phys. Rev. B 79 (2009) 1344371–1344378.
[29] B.F. Woodfield, J. Boerio-Goates, J.L. Shapiro, R.L. Putnam, A. Navrotsky, J. Chem. Thermodyn. 31 (1999) 245–253.
[30] J.C. Fernandes, F.S. Sarrat, R.B. Guimara~es, R.S. Freitas, M.A. Continentino, A. C. Doriguetto, Y.P. Mascarenhas, J. Ellena, E.E. Castellano, J.-L. Tholence, J. Dumas, L. Ghivelder, Phys. Rev. B 67 (2003) 1044131–1044137.
[31] M.V. Eremin, The Spectroscopy of the Crystals, Nayka, Leningrad, 1985, p.150.
[32] N.V. Kazak, M.S. Platunov, N.B. Ivanova, Yu. V. Knyazev, L.N. Bezmaternykh, E. V. Eremin, A.D. Vasil'ev, O.A. Bayukov, S.G. Ovchinnikov, D.A. Velikanov, Ya. V. Zubavichus, J. Exp. Theor. Phys. 117 (2013) 94–107.
[33] O.A. Bayukov, A.F. Savitskii, Phys. Stat. Sol. B 155 (1989) 249–255.
[34] J.E. Greedan, J. Mater. Chem 11 (2001) 37–53.